

# Back2Color: Domain-Adaptive Synthetic-to-Real Monocular Depth Estimation for Dynamic Traffic Scenes

Yufan Zhu, Chongzhi Ran, Mingtao Feng, Le Dong, *Member, IEEE*, Weisheng Dong, *Member, IEEE*, Antonio M. López, *Member, IEEE*

**Abstract**—Accurate monocular depth estimation is a fundamental component of vision-based perception systems in intelligent transportation applications. Despite recent progress, unsupervised monocular approaches still suffer from significant performance degradation in real-world traffic scenes due to synthetic-to-real domain gaps and the presence of dynamic, non-rigid objects such as vehicles and pedestrians. In this paper, we propose Back2Color, a robust unsupervised monocular depth estimation framework that addresses these challenges through domain adaptation and uncertainty-aware fusion. Specifically, Back2Color proposes a bidirectional depth-to-color transformation strategy that learns appearance mappings from real-world driving data and applies them to synthetic depth maps, thereby constructing training samples with realistic color appearance and paired synthetic depth. In this way, the proposed approach effectively reduces the domain gap between simulated and real traffic scenes, enabling the depth prediction network to learn more stable and generalizable priors. To further improve robustness under dynamic environments, we propose an auto-learning uncertainty temporal-spatial fusion (Auto-UTSF) module, which adaptively fuses complementary temporal and spatial cues by estimating pixel-wise uncertainty, enabling reliable depth prediction in the presence of moving objects and occlusions. Extensive experiments on challenging urban driving benchmarks, including KITTI and Cityscapes, demonstrate that the proposed method consistently outperforms existing unsupervised monocular depth estimation approaches, particularly in dynamic traffic scenarios, while maintaining high computational efficiency.

**Index Terms**—Computer vision, Deep Learning, Autonomous driving, Road transportation, Monocular depth estimation, Synthetic-to-real domain adaptation.

## I. INTRODUCTION

IN the real world, even after prolonged evolution, humans are still limited to qualitatively analyzing the depth of specific points in their field of view to assist in their actions [3]. Despite significant technological advances, the acquisition of precise and dense depth information remains a formidable challenge [4]–[9]. Even with the refinement of advanced LiDAR systems [5], their data are inherently sparse, comprising only discrete depth points. Unsupervised depth estimation (UDE), powered by triangulation [10] using purely visual

Yufan Zhu, Chongzhi Ran, Mingtao Feng, Le Dong, Weisheng Dong are with the School of Artificial Intelligence Xidian University, Xi'an 710071, China (e-mail: zhuyufan@xidian.edu.cn; czran@stu.xidian.edu.cn; mintfeng@hnu.edu.cn; dongle@xidian.edu.cn; wsdong@mail.xidian.edu.cn; gmshi@xidian.edu.cn).

Antonio M. López is with the Department of Computer Science and also with the Computer Vision Center (CVC), Universitat Autònoma de Barcelona (UAB), 08193 Bellaterra (Barcelona), Spain (e-mail: antonio@cvc.uab.cat).

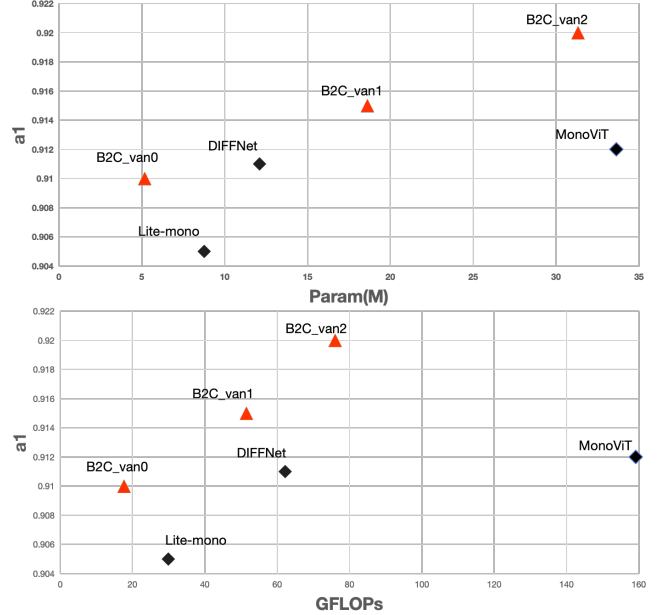


Fig. 1. Performance vs. methods efficiency on KITTI at a resolution of  $320 \times 1024$ . Our method (B2C) surpasses both the lightweight Lite-mono [1] and the highly effective MonoViT [2], excelling in both efficiency and accuracy.

approaches does not require additional annotation for depth information other than camera parameters. UDE eliminates the necessity of annotating depth labels for specific scenes. By utilizing binocular and motion disparity clues, it mimics the structure of human vision, making it efficient and cost-effective [11]. This is why many researchers and companies are actively pursuing this approach [12]. Monodepth2 [13], the most renowned framework for UDE, has established itself as a classic and successful method. By reprojecting related frames (temporal and spatial) and regressing depth values. This adaptability enables Monodepth2 to obtain depth information for various scenes through adaptive fine-tuning, making it highly versatile. However, despite its strengths, Monodepth2 has several limitations. Firstly, the auto-masking for handling non-rigid moving objects, follows the rule: the pixel error after reprojection should be less than before reprojection. This pixel-level determination cannot actively detect motion [14] and cannot ensure effectiveness in smooth regions. Additionally, when applied to more complex datasets such as Cityscapes [15], it almost fails. Secondly, photometric reprojection error also fails in areas with no texture or with texture-

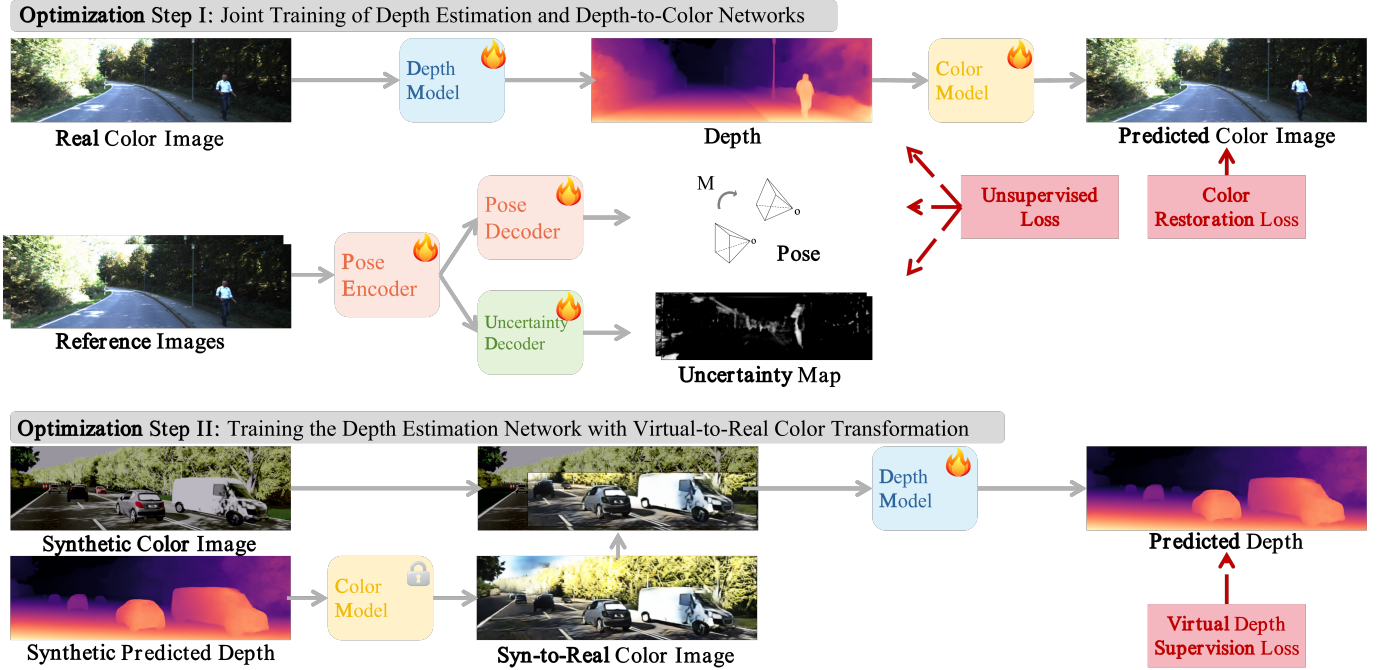


Fig. 2. **Illustration of the Back2Color training strategy.** In each iteration, the first stage jointly optimizes the depth estimation network and the depth-to-color network using real-world data with unsupervised photometric and color restoration losses. In the second stage, the depth-to-color network is fixed and applied to transform synthetic depth maps into realistic color images, enabling the depth estimation network to be trained with virtual depth supervision under a reduced domain discrepancy.

less background objects, leading to depth prediction failure. Lastly, methods based on photometric reprojection matching lack prior knowledge of the objective structure. These issues make it challenging for UDE methods to be applied in real world.

With the continuous advancement of computer graphics and virtual engine technologies, significant progress has been made in the creation and application of virtual urban scene datasets [15]–[19]. The evolution of 3D virtual engines, such as Unity and Unreal Engine [20], [21], has played a crucial role in enhancing the realism and visualization effects of virtual urban scenes. These engines not only facilitate finer scene modeling but also provide interactivity and dynamism, making virtual urban scene data more closely resemble the real world. Synthetic datasets can provide precise qualitative data for virtual urban scenes, including depth, semantic labels, and more. Therefore, it would be desirable if various synthetic scenes and dense depth could be used to assist in the UDE of the real-world [22]. Compared to synthetic datasets, real-world depth estimation datasets [15], [23] have the following notable drawbacks: firstly, synthetic depth data is dense, whereas depth data collected by LiDAR is sparse and discrete [23]. Secondly, depth computed through stereo matching suffers from occlusions and lacks accuracy due to the short baseline [15]. Additionally, sparse depth sampling does not provide sufficient information for learning when obstacles are small or distant (resulting in small apparent areas), making it challenging for the network to accurately reconstruct their shapes.

In this paper, we propose the Back2Color framework to address the appearance discrepancy between synthetic and real-world data in unsupervised monocular depth estimation.

Specifically, Back2Color introduces a bidirectional depth-to-color transformation strategy that learns appearance mappings from real-world driving scenes and applies them to synthetic depth maps. In this way, Back2Color constructs training pairs that combine realistic color appearance with corresponding synthetic depth, effectively narrowing the domain gap between simulated and real traffic scenes.

To further enable effective joint training across heterogeneous data sources, we introduce an enhanced CutMix strategy, termed Syn-Real CutMix [24], which mixes synthetic and syn-to-real images at both batch and spatial levels. This strategy enriches the training data with diverse color–depth associations derived from synthetic scenes while preserving real-world appearance characteristics. By jointly training on these complementary data sources, the proposed framework allows the depth estimation network to learn more stable and generalizable depth prediction priors, leading to improved robustness in real traffic environments.

In addition, we observe that existing auto-masking mechanisms often fail to reliably identify non-rigid moving objects in traffic scenes, especially when vehicles move at similar speeds or in opposite directions, which leads to erroneous depth predictions. To address this issue, we introduce an automatic uncertainty learning fusion strategy that combines temporal and spatial cues, termed Auto-learning Uncertainty Temporal-Spatial Fusion (Auto-UTSF) [25]. By explicitly modeling uncertainty, Auto-UTSF adaptively integrates complementary information from stereo and temporal supervision, enabling more reliable depth estimation under dynamic and occluded conditions.

To summarize, the main contributions of this work are as

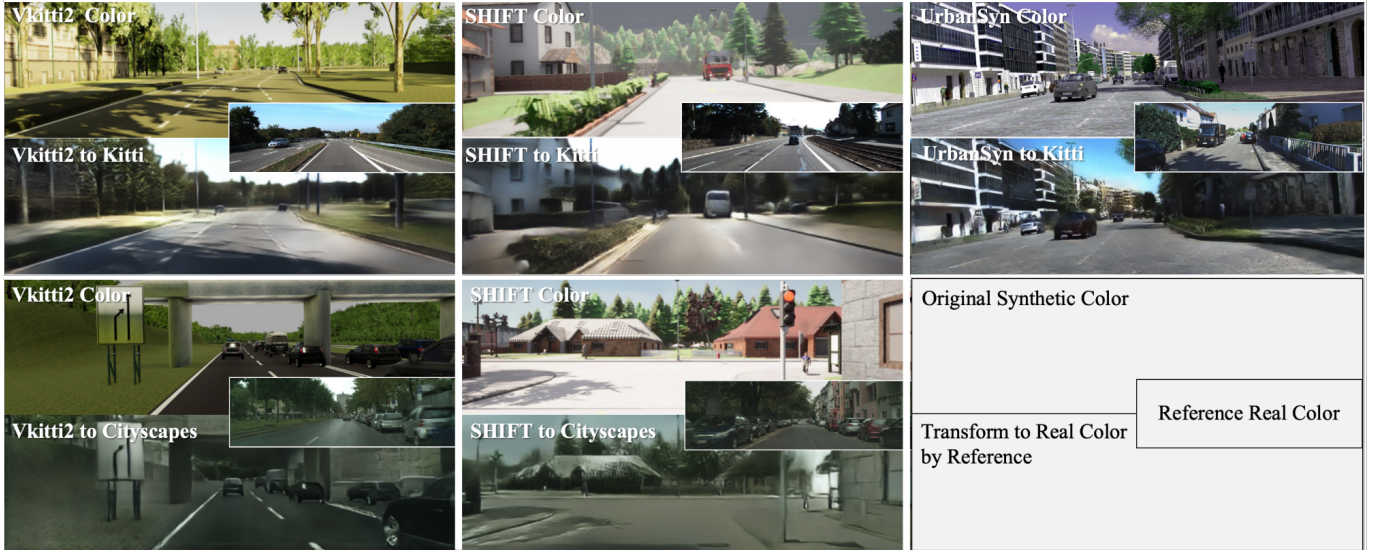


Fig. 3. **Color transformation for specific datasets:** we showcase the capability of our Back2Color framework to effectively transform various synthetic datasets, including vKITTI2 [16], SHIFT [26], and UrbanSyn [27], into Syn2Real images. These images closely emulate the real-world styles of KITTI [23], [28] and Cityscapes [15], demonstrating high fidelity and credibility.

follows:

- We propose Back2Color, a synthetic-to-real adaptation framework that learns scene-specific color information from real-world data and enables reverse color prediction from depth. Together with the proposed Syn-Real CutMix strategy, Back2Color effectively harmonizes joint training on synthetic and real datasets, improving the robustness of unsupervised monocular depth estimation in real traffic scenes.
- We introduce Auto-learning Uncertainty Temporal-Spatial Fusion (Auto-UTSF), which robustly handles non-rigid motion and occlusions by adaptively fusing complementary spatial and temporal supervision through uncertainty estimation.
- Extensive experiments on challenging urban driving benchmarks demonstrate that the proposed method consistently improves depth estimation accuracy while maintaining computational efficiency, and produces depth maps with clearer object boundaries.

## II. RELATED WORKS

### A. Unsupervised Depth Estimation

Unsupervised depth estimation aims to predict distances from stereo views or video sequences. Initial methods like those by Godard et al. [29] introduced disparity consistency loss, while Zhou et al. [30] pioneered depth and pose estimation simultaneously. Recent advancements [31]–[36] refine network structures for higher accuracy. Techniques like PackNet [31] and CADepth [32] enhance geometric and appearance information propagation. HR-Depth [33] and DIFFNet [34] utilize HRNet for better resolution utilization. RA-Depth [35] employs HRNet for both encoding and decoding. In natural language processing, the Transformer architecture [37] has been successful, later adapted to computer vision tasks [38], [39]. It serves as the backbone for depth estimation [1], [2],

[40]–[42], but faces challenges like computational demands and real-time constraints. Existing methods prioritize model architecture, often overlooking crucial obstacles and targets. Additionally, depth estimation models also face the issue of overfitting on specific datasets and a lack of continuous learning capability [43].

### B. Depth Estimation with Synthetic data

Researchers have already attempted to use synthesized dense depths to guide the training of real-world depth estimation [22], [44]. Gurram et al. [22] categorized this problem as a dimension adaptation problem, where the objective is to adapt models trained on a source(synthesized) domain to perform well in a different target domain(real-world). They employed the Gradient Reverse Layer [45] to identify features from different domains during back propagation. Swami et al. [44], on the other hand, simultaneously trained on both synthesized and real-world datasets, leveraging scale information in Synthetic dataset to recover scale in unsupervised depth estimation. To bridge the gap between real-world and synthetic datasets in the image domain, Zhao et al. [46] leveraged synthetically rendered data and employed image translation techniques to narrow the synthetic-real domain gap, thereby enhancing monocular depth prediction.

### C. Style transfer in urban scenes

Research on style transfer for urban scene images has long been ongoing due to its importance in autonomous driving technology. Isola et al. [47] proposed a conditional GAN framework for generating urban scene images from semantic segmentation images of Cityscapes in 2017. However, generative models may produce random and plausible objects, disrupting the scene structure, as shown in their experiments. Atapour et al. [48] utilized style transfer and adversarial training to convert real-world color images into synthetic

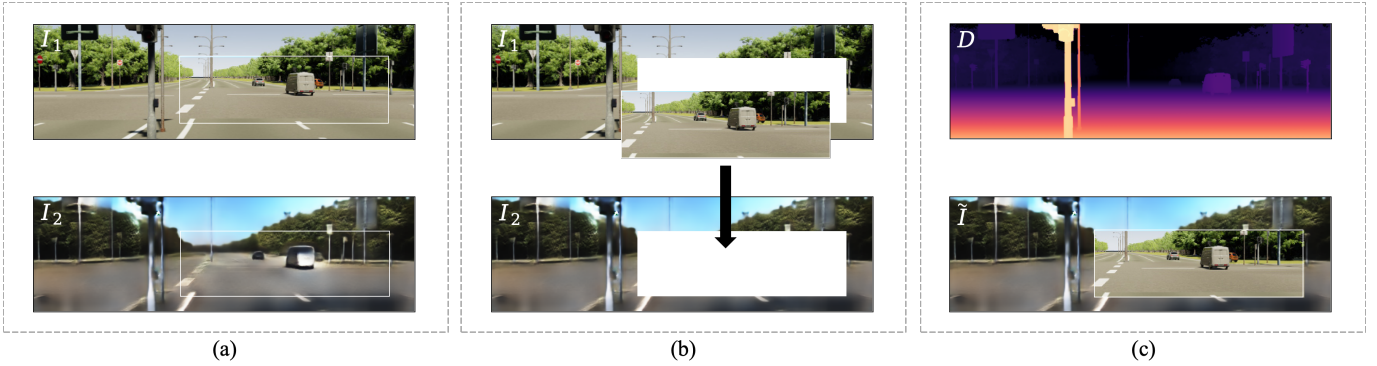


Fig. 4. **Syn-Real CutMix**: specific steps involved in our Syn-Real CutMix method for spatially combining colors: (a) Randomly select a rectangular region, denoted as  $M$ . (b) Replace the corresponding block in image  $I_2$  with the block from image  $I_1$ . (c) Resulting in the formation of new paired data  $(\tilde{I}, D)$ .

environment-style images. Huang et al. [49] applied GAN-based domain transfer for data augmentation in urban scene weather-time conversion. To minimize the gap between source and target domains, Gomez et al. [50] aligned colors across different domains in the Lab color space. Zheng et al. [51] used GANs to convert synthetic colors to real-world colors. With advancements in stable diffusion [52], [53], ControlNet [52] is now capable of generating images based on various conditions, including text, pose, Canny edges, and depth. This capability theoretically enables the generation of RGB images from urban depth maps, as demonstrated by RISHI et al. [53]. However, experiments [53] indicate that diffusion models do not strictly adhere to depth information and may arbitrarily alter target classes. Additionally, diffusion models require 2-5 seconds to generate a single image especially training with CNN model, and each condition demands extensive data for training. This makes it challenging to quickly fine-tune a depth estimation model for specific real-world scenarios. In contrast, our proposed ColorNet addresses these limitations, allowing for rapid deployment and real-time operation.

### III. METHODOLOGY

In this section, we present the Back2Color framework, which captures the depth-to-color mapping within the target domain and transfers synthetic colors to pseudo-realistic ones (III-A1). Back2Color is further enhanced with Real-Syn CutMix (III-A2) to jointly train for unsupervised depth estimation in the real world and supervised depth estimation in synthetic data. Then, we describe the Auto-learning Uncertainty Temporal-Spatial Fusion (Auto-UTSF) module (III-B), designed to address challenges associated with non-rigid motion. Throughout this paper, Depth and Disparity are considered equivalent.

#### A. Back to the Color

1) *Transform depth to specific colors*: the significant gap between synthetic and real-world color images arises from the inherent complexity of the real world. Colors in real-world scenes are influenced by various factors, including lighting intensity, surface material of obstacles, and smoothness, and can also be significantly degraded [54]. Each of these factors is intricate and highly variable, making them challenging to simulate realistically using typical 3D engines. As a result,

discerning the origin of an image intuitively is easy, both for humans and deep learning alike. Consequently, directly combining real-world and synthetic datasets for training essentially involves dealing with the integration issues of two distinct domains. Our Back2Color approach learns the mapping relationship in the target domain (Real). This mapping is then applied to the source domain (Synthetic) to reduce the gaps between colors of the source and target domains.

Objectively speaking, predicting color from 3D structural information constitutes a one-to-many mapping, a non-standard conditional generative tasks, where the same 3D structure can correspond to a multitude of different color images. However, under specific conditions, this seemingly impossible task becomes feasible: *Assuming that the color images in the target domain exhibit relatively high correlation*. The colors in real world datasets like Cityscapes and KITTI are notably different, as shown in Fig.3. Therefore, in order to bridge the substantial gap between synthetic  $\mathcal{S} \in \{\text{vKITTI2(vK)} [16], \text{SHIFT(SH)} [26], \text{UrbanSyn(Ur)} [27]\}$  and real-world  $\mathcal{X} \in \{\text{KITTI(KT)} [23], [28], \text{Cityscapes(Cs)} [15]\}$  datasets, we can learn the depth-to-color mapping in the target domain (real world color) and apply it to the source domain (synthetic color), thereby converting the source domain color to match those in the target domain. To bridge the appearance gap between synthetic and real-world data, we train a depth-to-color network  $\mathcal{F}_{d2c}$  that predicts color images from estimated depth maps in the real-world domain. Given a predicted depth map  $\hat{\mathbf{D}}_{\mathcal{X}}$  produced by the depth estimation network, the depth-to-color network reconstructs the corresponding color image as

$$\hat{\mathbf{I}}_{\mathcal{X}} = \mathcal{F}_{d2c}(\hat{\mathbf{D}}_{\mathcal{X}}; \theta_{d2c}), \quad (1)$$

where  $\theta_{d2c}$  denotes the learnable parameters of the depth-to-color network.

The reconstructed color image  $\hat{\mathbf{I}}_{\mathcal{X}}$  is supervised by the corresponding real color image  $\mathbf{I}_{\mathcal{X}}$  using a photometric reconstruction loss, defined as

$$\mathcal{L}_{d2c} = pe(\hat{\mathbf{I}}_{\mathcal{X}}, \mathbf{I}_{\mathcal{X}}), \quad (2)$$

where  $pe(\cdot, \cdot)$  denotes the photometric error function.

Next, we investigate whether the depth-to-color mapping learned from the real-world domain can be transferred to synthetic data. Specifically, after training the depth-to-color

network  $\mathcal{F}_{d2c}$  on real-world samples, we apply the learned model to predicted depth maps from the synthetic domain in order to generate color images that resemble the appearance characteristics of the target domain (e.g., KITTI), as illustrated in Fig. 3. Formally, given a predicted synthetic depth map  $\hat{\mathbf{D}}_S$ , the corresponding color image is generated as

$$\hat{\mathbf{I}}_{S \rightarrow \mathcal{X}} = \mathcal{F}_{d2c}(\hat{\mathbf{D}}_S; \theta_{d2c}), \quad (3)$$

where  $\hat{\mathbf{I}}_{S \rightarrow \mathcal{X}}$  denotes the synthetic color image transformed to match the appearance of the real-world domain.

2) *Syn-Real CutMix*: The objective of CutMix in our framework is to construct enhanced training pairs  $(\tilde{\mathbf{I}}, \mathbf{D})$  for improving robustness across domains. Unlike the original CutMix [24], which mixes two independent image-label pairs, the image pair used in our setting,  $(\mathbf{I}_S, \hat{\mathbf{I}}_{S \rightarrow \mathcal{X}})$ , represents two different color appearances corresponding to the same synthetic depth label  $\mathbf{D}_S$ . Therefore, we perform mixing only in the color space while keeping the depth supervision unchanged.

To introduce spatial diversity, as illustrated in Fig. 4, we denote the image pair  $(\mathbf{I}_S, \hat{\mathbf{I}}_{S \rightarrow \mathcal{X}})$  as  $(\mathbf{I}_1, \mathbf{I}_2)$ , which are randomly swapped with equal probability. A rectangular region with height and width larger than half of the original image is then randomly cropped from  $\mathbf{I}_1$  and replaced with the corresponding region from  $\mathbf{I}_2$ , yielding the mixed image

$$\tilde{\mathbf{I}} = \mathbf{M} \odot \mathbf{I}_1 + (1 - \mathbf{M}) \odot \mathbf{I}_2, \quad (4)$$

where  $\mathbf{M} \in \{0, 1\}^{H \times W}$  denotes a binary mask indicating the preserved and replaced regions, and  $\odot$  represents element-wise multiplication.

The Syn-Real enhanced images  $\tilde{\mathbf{I}}$  are then combined with real-world target images  $\mathbf{I}_{\mathcal{X}}$  within the same training batch. This joint batching strategy allows the monocular depth estimation network to be trained simultaneously on real-world, synthetic, and Syn-to-Real samples. The spatial randomization introduced by Syn-Real CutMix further encourages the network to focus on structural cues rather than specific color appearances, thereby improving generalization across domains.

### B. Auto-learning Uncertainty Temporal-Spatial Fusion

During the evaluation of the Back2Color framework, we observe that the widely adopted auto-masking strategy [13] often fails in complex urban scenes, particularly on the Cityscapes dataset, as illustrated in Fig. 5. By inspecting the auto-masking outputs, we find that non-rigid moving objects, such as vehicles and pedestrians, cannot be reliably filtered. This limitation is further aggravated by the complexity of real-world traffic scenes and the strong fitting capability of modern depth networks, which may compensate for non-rigid motion by adjusting depth predictions to remain consistent with camera poses [55]. Moreover, masking strategies based on optical flow [25] completely fail for objects moving in the opposite direction of the ego-motion, as shown in Fig. 5.

In temporal sequences, freely moving objects violate the rigid-scene assumption underlying depth- and pose-based reprojection, as depicted in Fig. 6. Auto-masking attempts to

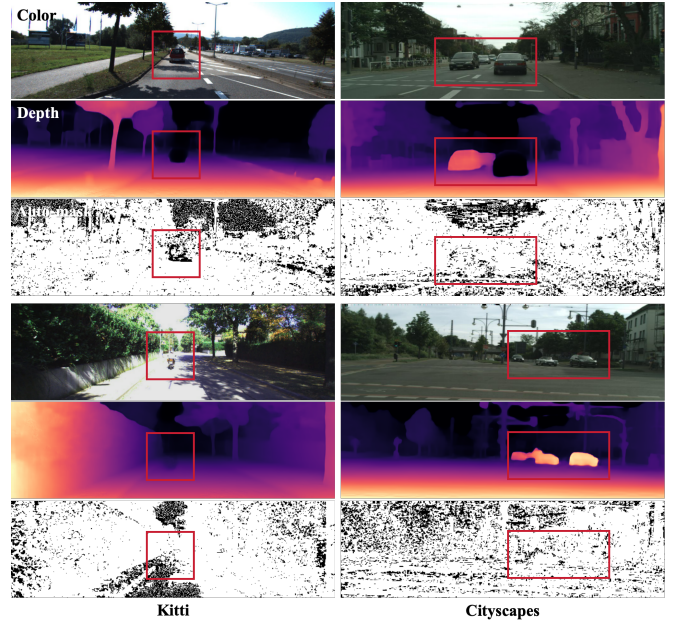


Fig. 5. When network capabilities become stronger, and the number of non-rigid objects in the dataset increases, the shortcomings [25] of Auto-masking and Minimum Reprojection Error lead to the reappearance of errors.

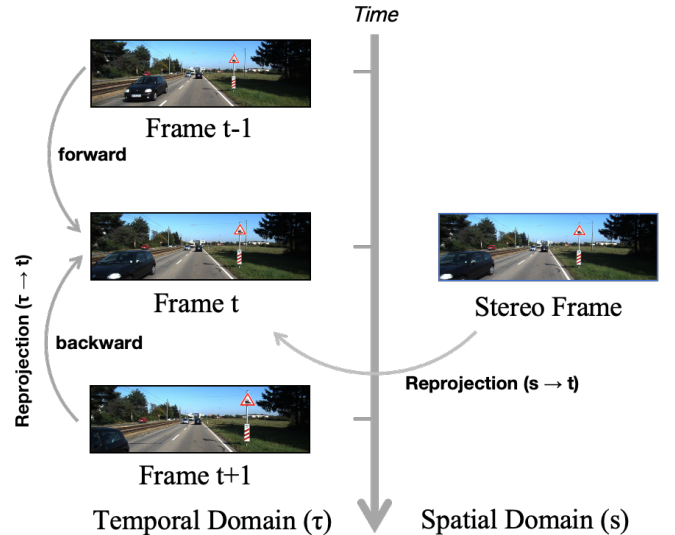


Fig. 6. Illustrates the complementary characteristics of temporal and spatial reprojection, which motivates the proposed Auto-UTSF strategy.

identify such pixels by comparing reprojection errors before and after geometric warping:

$$\mu_i = \mathbb{I} \left[ \min_k pe(\mathbf{I}_t, \mathbf{I}_{k \rightarrow t}) < \min_k pe(\mathbf{I}_t, \mathbf{I}_k) \right], \quad (5)$$

where  $k \in \{t-1, t+1\}$ . However, this heuristic is insufficient when depth predictions can be adjusted to rationalize non-rigid motion, leading to incorrect supervision.

Notably, non-rigid motion only affects temporally adjacent frames, whereas in spatially related stereo pairs captured at the same time, such motion does not occur. Therefore, instead of simply excluding unreliable pixels, introducing spatial (stereo) supervision provides a more direct and effective solution. Nevertheless, temporal and spatial reprojections exhibit complementary characteristics. Temporal reprojection benefits from larger baselines and multi-frame context, making it suitable

for distant regions and occlusion completion, while spatial reprojection offers reliable supervision for non-rigid objects but suffers from limited baseline and asymmetric occlusions. These observations motivate a unified strategy that adaptively fuses temporal and spatial supervision.

Inspired by uncertainty learning [25], [56], [57], we introduce an Auto-learning Uncertainty Temporal–Spatial Fusion (Auto-UTSF) mechanism to combine temporal and spatial reprojection losses.

In this section, subscripts  $t$ ,  $t-1$ ,  $t+1$ , and  $s$  are used to index temporal and stereo frames, while dataset/domain subscripts (e.g.,  $\mathcal{X}$  and  $\mathcal{S}$ ) are omitted for clarity when the context is unambiguous. And  $i$  indexes individual pixels in the image, and  $N$  denotes the total number of pixels. Following [25], pixel-wise temporal uncertainty logits  $\hat{u}_{i,k}^\tau$  are predicted for temporally adjacent frames  $k \in \{t-1, t+1\}$  and normalized using a softmax operation:

$$u_{i,k}^\tau = 1 - \text{Softmax}(\hat{u}_{i,t-1}^\tau, \hat{u}_{i,t+1}^\tau), \quad \sum_k u_{i,k}^\tau = 1. \quad (6)$$

And The temporal reprojection loss is then defined as

$$\mathcal{L}_\tau = \frac{1}{N} \sum_i \sum_k u_{i,k}^\tau pe(\mathbf{I}_t, \mathbf{I}_{k \rightarrow t}) + \alpha \frac{1}{N} \sum_i \sum_k \hat{u}_{i,k}^\tau, \quad (7)$$

where  $\alpha$  is set to  $1 \times 10^{-2}$ .

To further fuse temporal and spatial supervision, we introduce domain-level uncertainty to balance their contributions. Temporal-domain and spatial-domain uncertainty logits ( $\hat{u}_i^\tau, \hat{u}_i^s$ ) are normalized as

$$u_i^\tau, u_i^s = 1 - \text{Softmax}(\hat{u}_i^\tau, \hat{u}_i^s), \quad u_i^\tau + u_i^s = 1. \quad (8)$$

The final uncertainty-aware temporal–spatial fusion loss is formulated as

$$\begin{aligned} \mathcal{L}_{ud} = & \frac{1}{N} \sum_i \left( u_i^\tau \sum_k u_{i,k}^\tau pe(\mathbf{I}_t, \mathbf{I}_{k \rightarrow t}) \right. \\ & \left. + u_i^s pe(\mathbf{I}_t, \mathbf{I}_{s \rightarrow t}) \right) \\ & + \alpha \frac{1}{N} \sum_i \left( \sum_k \hat{u}_{i,k}^\tau + \hat{u}_i^\tau + \hat{u}_i^s \right), \end{aligned} \quad (9)$$

where  $\mathbf{I}_s$  denotes the stereo source image corresponding to the target frame  $\mathbf{I}_t$ .

Through uncertainty learning, the model automatically assigns low weights to unreliable regions in each domain. In temporal reprojection, high uncertainty mainly corresponds to occlusions and non-rigid motion, while in spatial reprojection, uncertainty primarily arises from occluded regions caused by viewpoint changes. By fusing uncertainties from both temporal and spatial domains, Auto-UTSF selectively suppresses unreliable supervision and exploits complementary geometric cues, enabling robust depth estimation in dynamic traffic scenes.

### C. Training Strategy

1) *Synthetic supervised depth loss*: Since unsupervised depth estimation models based on video sequences cannot recover scale information, we adopt the affine-invariant mean absolute error loss used by MiDas [58] and Depth Anything

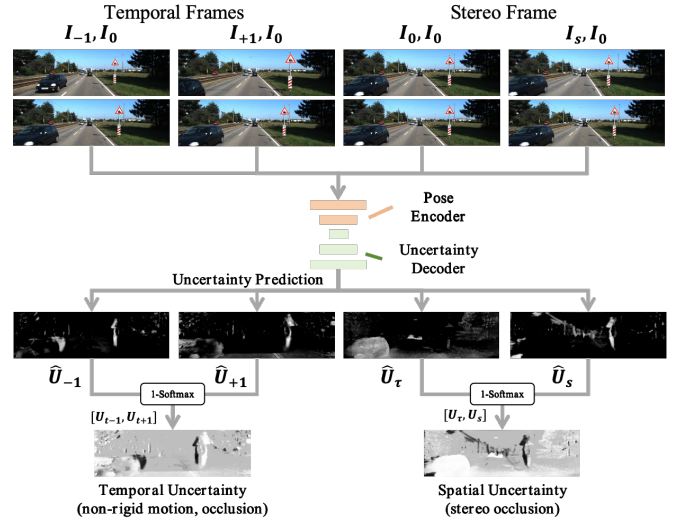


Fig. 7. **Auto-Spatio-Temporal Uncertainty Fusion**: Given temporal and stereo frame pairs, the uncertainty generation module predicts pixel-wise uncertainty logits, which are normalized via a  $1 - \text{Softmax}$  operation to adaptively weight temporal and spatial reprojection errors.

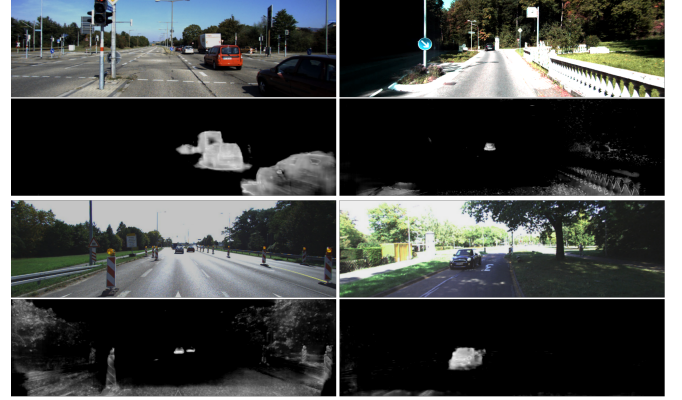


Fig. 8. **Temporal Uncertainty for non-rigid objects**: We can identify non-rigid objects by predicting the uncertainty during the training process, thereby eliminating their impact in the training. The fine-grained recognition can even identify very small non-rigid targets.

[59] for joint training with synthesized depth, which has deterministic values varying with different camera parameters:

$$\mathcal{L}_{sd} = \frac{1}{HW} \sum_i |d_i^* - \hat{d}_i^*|, \quad (10)$$

where  $d_i^*$  and  $\hat{d}_i^*$  are the scaled and shifted pixels of predicted  $\hat{\mathbf{D}}$  and synthetic groundtruth  $\mathbf{D}$ .

$$d_i^* = \frac{d_i - \text{median}(\mathbf{D})}{s(\mathbf{D})}, \quad s(\mathbf{D}) = \frac{1}{HW} \sum_i |d_i - \text{median}(\mathbf{D})|. \quad (11)$$

2) *Optimization Strategy*: Swami et al. [44] pointed out that, in unsupervised domain adaptation methods, multiple networks and optimization objectives often compete with each other, thereby failing to jointly contribute to effective depth estimation. Such a lack of cooperation among different components makes optimization challenging and limits overall performance.

To address this issue, we adopt two separate optimizers to decouple the training process and independently optimize the Depth Network on synthetic data and real-world unsupervised data, respectively, as illustrated in Fig. 2. Each training batch



Fig. 9. **The synthetic datasets:** In vKITTI2, depth cannot penetrate transparent entities such as glass windows, whereas in the SHIFT dataset, depth can penetrate transparent entities. SHIFT and UrbanSyn includes simulated pedestrians. And UrbanSyn is the synthetic dataset that most closely resembles real world.

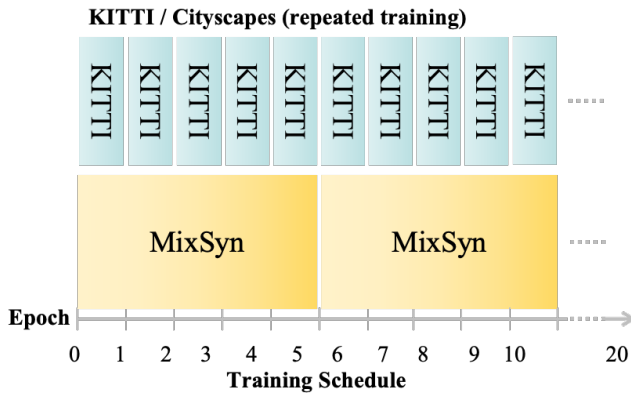


Fig. 10. **The MixSyn dataset** contains more samples than the real-world unsupervised datasets, requiring it to be divided into multiple epochs. While the MixSyn dataset is trained once, the real-world unsupervised datasets may be trained multiple times.

contains both real-world samples for unsupervised depth estimation and synthetic color samples.

**Optimizer Step I:** The Depth Network is trained in an unsupervised manner on real-world samples using our proposed Auto-UTSF mechanism, while the Color Network is trained in a supervised manner on real-world data to predict color from depth. We set  $\gamma = 10^{-3}$ , and  $\mathcal{L}^{\text{sm}}$  denotes the smoothness loss. The overall loss for this step is defined as

$$\mathcal{L}_{\mathcal{O}_1} = \mathcal{L}_{\text{d2c}} + \mathcal{L}_{\text{ud}} + \gamma \mathcal{L}^{\text{sm}}. \quad (12)$$

**Optimizer Step II:** The Depth Network is further trained in a supervised manner using the proposed Syn-Real CutMix samples. The corresponding optimization objective is given by

$$\mathcal{L}_{\mathcal{O}_2} = \mathcal{L}_{\text{sd}} + \gamma \mathcal{L}^{\text{sm}}. \quad (13)$$

TABLE I  
EXPERIMENTS ON THE KITTI EIGEN SPLIT USING ONLY THE MONOCULAR SEQUENCE DATASET FOR TRAINING.

Method	Sup. <sup>1</sup>	Size	Error Metric				Accuracy Metric		
			abs_rel	sq_rel	rmse	rmse_log	a1	a2	a3
Monodepth2 [13]	m	192×640	0.115	0.903	4.863	0.193	0.877	0.959	0.981
CADepth [32]	m	192×640	0.105	0.769	4.535	0.181	0.892	0.964	0.983
DIFFNet [34]	m	192×640	0.102	0.749	4.445	0.179	0.897	0.965	0.983
MonoFormer [60]	m	192×640	0.106	0.839	4.627	0.183	0.889	0.962	0.983
Lite-Mono [1]	m	192×640	0.101	0.729	4.454	0.178	0.897	0.965	0.983
MonoViT [2]	m	192×640	0.099	0.708	4.372	0.175	0.900	0.967	<b>0.984</b>
Back2Color	m	192×640	<b>0.096</b>	<b>0.708</b>	<b>4.307</b>	<b>0.173</b>	<b>0.905</b>	<b>0.968</b>	<b>0.985</b>
DIFFNet [34]	m	320×1024	0.097	0.722	4.345	0.174	0.907	0.967	0.984
Lite- [1]	m	320×1024	0.097	0.710	4.309	0.174	0.905	0.967	0.984
MonoViT [2]	m	320×1024	0.096	0.714	4.292	0.172	0.908	0.968	0.984
Back2Color	m	320×1024	<b>0.093</b>	<b>0.687</b>	<b>4.171</b>	<b>0.168</b>	<b>0.912</b>	<b>0.970</b>	<b>0.985</b>

## IV. EXPERIMENTS

In this section, we initially establish the superiority of our Back2Color by comparing it with other state-of-the-art (SoTA) approaches on the KITTI Eigen split and Cityscapes depth estimation benchmark (Tab.I, Tab.II, and Tab.IV). Following this, we conduct ablation experiments to analyze the effects of the proposed methods (Tab.VIII, Tab.VII and Tab.VI). Additionally, we compare our approach with other methods that utilize synthetic datasets (Tab.V), perform comparisons at higher resolutions (Tab.III), and benchmark against the lightest and most effective methods (Tab.IX). At the same time, we present some visual results of our method on the KITTI and Cityscapes datasets (Fig. 11, Fig. 12, and Fig. 13).

### A. Datasets

We utilized two unsupervised monocular depth estimation datasets: KITTI [28] and Cityscapes [15], along with synthetic datasets vKITTI2 [16], SHIFT [26], and UrbanSyn [27]. **KITTI** contains 39,810 training triplets, 4,424 for validation, and 697 for evaluation, featuring diverse scenes with rich colors and occasional non-rigid objects. **Cityscapes**, designed for autonomous driving, provides 69,731 monocular triplets from the LeftImg8bit Sequence for training, mainly urban scenes with non-rigid pedestrians and vehicles, often in darker tones. The baseline for KITTI stereo data is 54 cm, while for Cityscapes it is 22 cm. **vKITTI2**, an upgraded version of Virtual KITTI, uses the Unity game engine for a more photorealistic environment and provides 21,260 frames for training. **SHIFT** features various weather conditions and times, offers dense depth information with 1 mm resolution, and includes simulated pedestrians. We selected 153,000 frames and synthetic depths from its front-view cameras. **UrbanSyn**, designed to address the synth-to-real domain gap, provides 7,539 images with depth labels, offering a highly realistic synthetic dataset for various computer vision tasks.

To leverage the variety of multiple synthetic datasets, we normalized and shuffled the specifications (size, depth resolution, etc.) of the vKITTI2, SHIFT, and UrbanSyn datasets to create a unified dataset called **MixSyn**. The MixSyn dataset contains significantly more samples compared to KITTI and Cityscapes. Therefore, during the training process, MixSyn is trained once, while KITTI or Cityscapes is trained for multiple epochs, as shown in Fig.10. We demonstrate the advantages of using MixSyn in Tab. VIII.

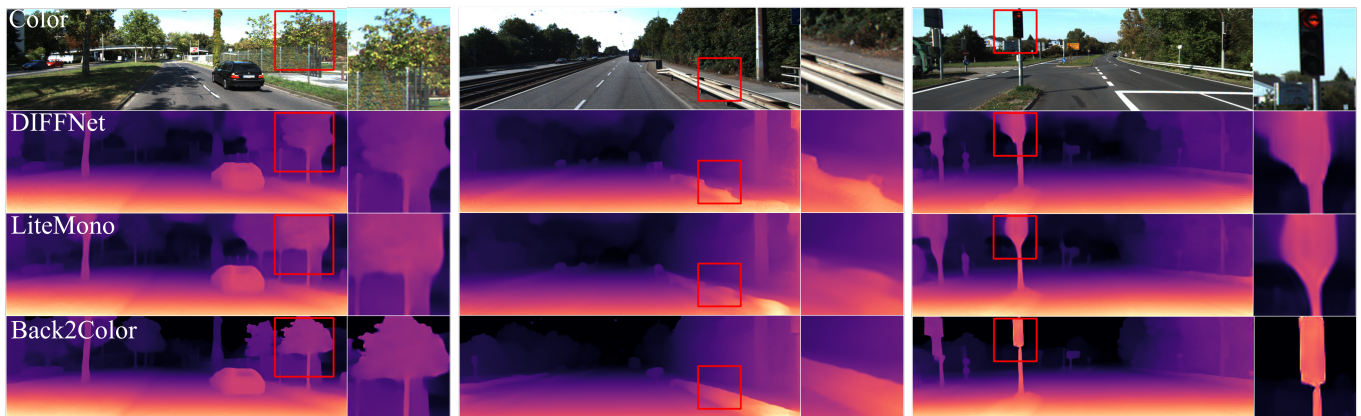


Fig. 11. **Visual of Depth Estimation on KITTI:** Our method yields clearer depth estimates with higher correlation to corresponding colors, sharper boundaries, and fewer areas with chaotic depth clouds.

### B. Implementation Details

All experiments are implemented using PyTorch [61] and conducted on a single NVIDIA RTX 3090Ti GPU with 24 GB memory. We adopt the Adam optimizer [62] with an initial learning rate of  $1 \times 10^{-4}$ , following the setting of Monodepth2 [13]. The learning rate is decayed to  $1 \times 10^{-5}$  after 15 epochs, while the remaining hyperparameters are set to  $(\beta_1, \beta_2) = (0.9, 0.999)$ . The SSIM loss weight is set to 0.85, and the smoothness regularization weight is set to  $\alpha = 1 \times 10^{-3}$ . Depth estimation performance is evaluated using standard metrics [28], including AbsRel, SqRel, RMSE,  $\text{RMSE}_{\log}$ , and accuracy thresholds.

To ensure computational efficiency and real-time applicability in urban driving scenarios, we adopt a lightweight CNN-based backbone for feature extraction, specifically the Visual Attention Network (VAN) [63], which captures long-range dependencies with low computational cost. A minor architectural adaptation is introduced to preserve higher-resolution features for dense depth prediction, while keeping the original backbone structure unchanged. The extracted multi-level features are subsequently processed by a high-resolution depth decoder [35] to recover fine-grained spatial details and generate depth maps at the input resolution. Experimental results demonstrate that the proposed framework consistently outperforms commonly used CNN-based backbones, such as ResNet-34, HRDepth, and DIFFNet, and achieves competitive performance compared to Transformer-based methods [1], [2] with significantly lower computational complexity. VAN0-VAN3 denote four variants of the VAN backbone with different parameter scales, as summarized in Table IX. Although VAN is adopted as the default backbone for efficiency, Experimental results demonstrate that the proposed framework consistently improves performance when integrated with commonly used CNN-based backbones, such as ResNet-34, HRDepth, and DIFFNet, and achieves competitive performance compared to Transformer-based methods [1], [2] with significantly lower computational complexity, as shown in Fig. IX.

<sup>1</sup>Sup.(Supervision) in the tables means what training set is used, Video(m),Stereo(s).

TABLE II  
EXPERIMENTS ON THE KITTI EIGEN SPLIT USING ONLY THE MONOCULAR SEQUENCE AND STEREO DATASETS FOR TRAINING.

Method	Sup. <sup>1</sup>	Size	Error Metric				Accuracy Metric		
			abs_rel	sq_rel	rmse	rmse_log	a1	a2	a3
Monodepth2 [13]	ms	192×640	0.106	0.818	4.750	0.196	0.874	0.957	0.979
HR-Depth [33]	ms	192×640	0.107	0.785	4.612	0.185	0.887	0.962	0.982
CADepth [32]	ms	192×640	0.102	0.752	4.504	0.181	0.894	0.964	0.983
DIFFNet [34]	ms	192×640	0.101	0.749	4.445	0.179	0.898	0.965	0.983
MonoViT [2]	ms	192×640	0.098	0.683	4.333	0.174	0.904	0.967	<b>0.984</b>
Back2Color	ms	192×640	<b>0.092</b>	<b>0.685</b>	<b>4.229</b>	<b>0.170</b>	<b>0.911</b>	<b>0.968</b>	<b>0.984</b>
Monodepth2 [13]	ms	320×1024	0.106	0.806	4.630	0.193	0.876	0.958	0.980
HR-Depth [33]	ms	320×1024	0.101	0.716	4.395	0.179	0.894	0.966	0.983
CADepth [32]	ms	320×1024	0.096	0.694	4.264	0.173	0.908	0.968	0.984
DIFFNet [34]	ms	320×1024	0.094	0.678	4.250	0.172	0.911	0.968	0.984
MonoViT [2]	ms	320×1024	0.093	0.671	4.202	0.169	0.912	0.969	0.984
Back2Color	ms	320×1024	<b>0.087</b>	<b>0.644</b>	<b>4.079</b>	<b>0.166</b>	<b>0.920</b>	<b>0.970</b>	<b>0.985</b>

TABLE III  
EXPERIMENTS ON THE KITTI EIGEN SPLIT AT 384 × 1280 RESOLUTION.

Method	Sup. <sup>1</sup>	Error Metric				Accuracy Metric		
		abs_rel	sq_rel	rmse	rmse_log	a1	a2	a3
PackNet-SFM [31]	m	0.107	0.802	4.538	0.186	0.889	0.962	0.981
SGDepth [64]	m	0.107	0.768	4.468	0.186	0.891	0.963	0.982
MonoViT [2]	m	0.094	0.682	4.200	0.170	0.912	0.969	0.984
PlaneDepth [65]	ms	0.090	<b>0.584</b>	4.130	0.182	0.896	0.962	0.981
Back2Color	ms	<b>0.086</b>	0.629	<b>4.054</b>	<b>0.165</b>	<b>0.920</b>	<b>0.970</b>	<b>0.985</b>

### C. Monocular Depth Estimation Performance

Our recommended experimental setup is to use the VAN2 model (balancing efficiency and performance), utilize the MixSyn synthetic dataset, and employ spatiotemporal supervision (ms). If there are no annotations, the results should be based on this setup. The evaluation results are summarized in Tab.I and Tab.II with KITTI Eigen Split [28] and Tab.IV with Cityscapes benchmark, followed by an illustration of their performance qualitatively in Fig.11 and Fig.12. Our method outperforms all existing SoTA unsupervised approaches, including some based on transformer [1], [2] with larger params and more complex structures(Tab.IX).

### D. Ablation Study

As illustrated in Tab. VII, we conducted experiments on our Back2Color framework by replacing different network structures to demonstrate the effectiveness of our new framework. The results also demonstrated that using a pre-trained checkpoint enhances the network’s ability to process natural

TABLE IV  
EXPERIMENTS ON THE CITYSCAPES BENCHMARK AT 192×640.  
METHODS\* REQUIRE SEMANTIC INFORMATION, AND BACK2COLOR  
REQUIRES STEREO PAIRS DURING TRAINING.

Method	Error Metric				Accuracy Metric		
	abs_rel	sq_rel	rmse	rmse_log	a1	a2	a3
Struct2Depth* [66]	0.145	1.737	7.280	0.205	0.813	0.942	0.976
GLNet [67]	0.129	1.044	5.361	0.212	0.843	0.938	0.976
Gordon et al.* [68]	0.127	1.330	6.960	0.195	0.830	0.947	0.981
Li et al. [69]	0.119	1.290	6.980	0.190	0.846	0.952	0.982
Lee et al.* [70]	0.111	1.158	6.437	0.182	0.868	0.961	0.983
RM-Depth [55]	0.090	0.825	5.503	0.143	0.913	0.980	0.993
<b>Back2color</b>	<b>0.076</b>	<b>0.784</b>	<b>5.159</b>	<b>0.127</b>	<b>0.937</b>	<b>0.984</b>	<b>0.994</b>

TABLE V  
EXPERIMENTS WITH METHODS USING THE SYNTHETIC DATASET  
(VKITTI2) AT 192×640 RESOLUTION AND TRAINING WITH MONOCULAR  
SEQUENTIAL ONLY.

Method	Size	Error Metric				Accuracy Metric		
		abs_rel	sq_rel	rmse	rmse_log	a1	a2	a3
MonoDEVSNet [22]	192×640	0.102	<b>0.685</b>	<b>4.303</b>	0.178	0.894	0.966	<b>0.984</b>
Back2Color	192×640	<b>0.096</b>	0.708	4.307	<b>0.173</b>	<b>0.905</b>	<b>0.968</b>	<b>0.984</b>
Swami et al. [44]	320×1024	0.103	<b>0.654</b>	4.300	0.178	0.891	0.966	0.984
Back2Color	320×1024	<b>0.093</b>	0.687	<b>4.171</b>	<b>0.168</b>	<b>0.912</b>	<b>0.970</b>	<b>0.985</b>

images, significantly benefiting depth estimation. Next, we conducted ablation experiments to separately evaluate each of the proposed modules, as shown in Tab.VI including the MixSyn dataset, the Back2Color training framework, and the auto-learning uncertainty temporal-spatial fusion method (UTSF). The results demonstrated that simply combining real and synthetic data for training did not improve performance. However, applying the Back2Color framework for color domain adaptation effectively addressed this issue. Additionally, Auto-UTSF further improved performance by leveraging advantageous information from both the temporal and spatial domains.

Then we compared our method with other novel approaches also joint training with synthetic datasets. Our improvement remains significant in comparison, as shown in Tab.V.

Additionally, we used various synthetic datasets such as vKITTI2, SHIFT, and UrbanSyn to real-world unsupervised depth model training, as shown in Tab.VIII. The results consistently achieved excellent improvement, demonstrating the strong adaptability of our method. To demonstrate that the improvement in our Back2Color method is not due to the increased training samples (Synthetic Datasets) but rather due to the diverse priors brought by various synthetic datasets, we conducted experiments using 20% and 50% synthetic samples (Rows 6, 7, and Rows 9, 10) while ensuring the total number of dataset samples remains the same as the KITTI dataset

TABLE VI  
ABLATION EXPERIMENTS TO TEST DIFFERENT MODULES. THE  
EXPERIMENTS USE A STEREO SETUP(MS) WITH A RESOLUTION OF  
320×1024. ROW 1 SHOWS THE RESULTS OF MONODEPTH2 [13] AS A  
REFERENCE.

Modules	Error Metric				Accuracy Metric		
	abs_rel	sq_rel	rmse	rmse_log	a1	a2	a3
Backbone	0.094	0.703	4.435	0.173	0.909	0.969	0.984
Backbone+MixSyn	0.095	0.724	4.672	0.172	0.910	0.969	0.984
Backbone+MixSyn+B2C	0.090	0.688	4.320	0.169	0.915	<b>0.970</b>	<b>0.985</b>
Backbone+MixSyn+B2C+UTSF	<b>0.087</b>	<b>0.644</b>	<b>4.079</b>	<b>0.166</b>	<b>0.920</b>	<b>0.970</b>	<b>0.985</b>

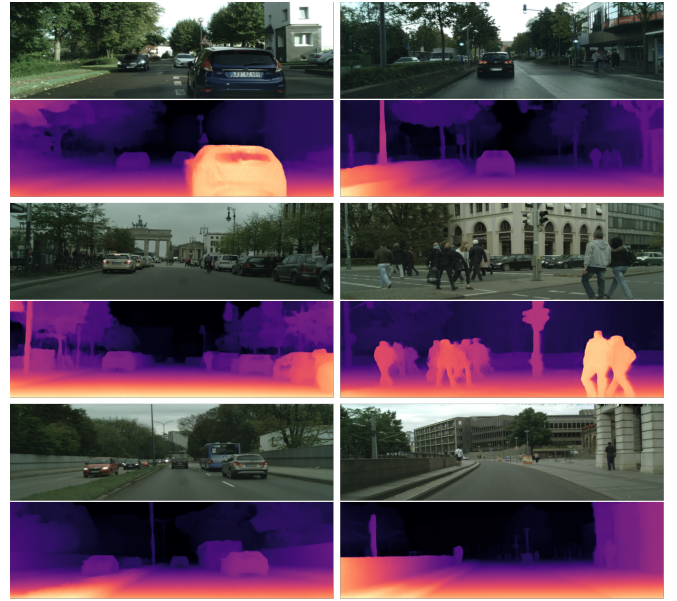


Fig. 12. The visual results on Cityscapes: Our method yields clearer depth estimates with higher correlation to corresponding colors, sharper boundaries, and fewer areas with chaotic depth clouds.

TABLE VII  
EXPERIMENTS ON THE KITTI EIGEN SPLIT AT 192×640 RESOLUTION.  
RESULTS SHOW THAT BACK2COLOR CONSISTENTLY IMPROVES  
PERFORMANCE ACROSS DIFFERENT BACKBONES, INDICATING THAT THE  
GAIN IS NOT SOLELY ATTRIBUTED TO BACKBONE SELECTION. VAN\*  
DENOTES TRAINING WITHOUT IMAGE NET PRETRAINING.

Method	Model	Error Metric				Accuracy Metric		
		abs_rel	sq_rel	rmse	rmse_log	a1	a2	a3
Monodepth2 [13]	Resnet34	0.106	0.818	4.750	0.196	0.874	0.957	0.979
Back2Color	Resnet34	<b>0.104</b>	<b>0.808</b>	<b>4.617</b>	<b>0.186</b>	<b>0.883</b>	<b>0.962</b>	<b>0.982</b>
HRDepth [33]	HRDepth	0.107	0.785	4.612	0.185	<b>0.887</b>	0.962	0.982
Back2Color	HRDepth	<b>0.105</b>	<b>0.745</b>	<b>4.469</b>	<b>0.182</b>	<b>0.887</b>	<b>0.964</b>	<b>0.984</b>
DIFNet [34]	DIFNet	0.101	0.749	4.445	0.179	0.898	0.965	0.983
Back2Color	DIFNet	<b>0.094</b>	<b>0.660</b>	<b>4.254</b>	<b>0.172</b>	<b>0.904</b>	<b>0.967</b>	<b>0.984</b>
Back2Color	VAN2*	0.123	0.997	4.996	0.202	0.858	0.953	0.979
Back2Color	VAN2	<b>0.092</b>	<b>0.685</b>	<b>4.229</b>	<b>0.170</b>	<b>0.911</b>	<b>0.968</b>	<b>0.984</b>

(39,810). The results are consistent with those obtained using the full dataset, proving that the enhancement of our method is not due to the increase in training samples. Additionally, when using the MixSyn mixed synthetic dataset, some metrics (rmse\_log and a1) show significant improvement compared to using a single dataset, demonstrating that our method benefits from learning the variety of multiple synthetic datasets.

Finally, to demonstrate the exceptional efficiency of our model, we compared it with the current best-performing MonoViT [2] and the lightweight Lite-mono [1]. Our VAN0 model is not only lighter than Lite-mono but also delivers superior performance. Additionally, it achieves competitive results with only one-sixth of the parameters of MonoViT. Meanwhile, our VAN2 model, which has a parameter count similar to MonoViT, shows a significant performance improvement, making it the current state-of-the-art (SOTA) model.

### E. Visualization Analysis

The impact of synthetic datasets can be analyzed by comparing the joint training with different synthetic datasets, as shown in the Fig.13.

TABLE VIII  
ABLATION STUDY ON THE IMPACT OF VARIOUS SYNTHETIC DATASETS.

Size	Syn	Number of Samples				Error Metric				Accuracy Metric		
		KITTI	vKITTI2	SHIFT	UrbanSyn	abs_rel	sq_rel	rmse	rmse_log	a1	a2	a3
<b>192×640</b>	<b>vKITTI2</b>	39810	21260	0	0	0.094	0.694	4.296	0.173	0.907	0.968	0.984
<b>192×640</b>	<b>SHIFT</b>	39810	0	153000	0	<b>0.092</b>	0.676	4.238	0.171	0.909	<b>0.969</b>	0.984
<b>192×640</b>	<b>UrbanSyn</b>	39810	0	0	7539	0.093	<b>0.644</b>	<b>4.198</b>	0.172	0.907	0.968	0.984
<b>192×640</b>	<b>MixSyn</b>	39810	21260	153000	7539	<b>0.092</b>	0.685	4.229	<b>0.170</b>	<b>0.911</b>	0.968	0.984
<b>320×1024</b>	<b>vKITTI2</b>	39810	21260	0	0	0.090	0.677	4.173	0.169	0.914	0.969	0.984
<b>320×1024</b>	<b>vKITTI2</b>	31848	7962	0	0	0.090	0.675	4.143	0.168	0.917	0.970	0.985
<b>320×1024</b>	<b>vKITTI2</b>	19905	19905	0	0	0.091	0.684	4.192	0.169	0.913	0.969	0.985
<b>320×1024</b>	<b>SHIFT</b>	39810	0	153000	0	0.089	0.651	4.158	0.167	0.916	0.970	0.985
<b>320×1024</b>	<b>SHIFT</b>	31848	0	7962	0	0.090	0.684	4.158	0.168	0.916	0.970	0.984
<b>320×1024</b>	<b>SHIFT</b>	19905	0	19905	0	0.090	0.680	4.144	0.167	0.915	0.970	0.985
<b>320×1024</b>	<b>UrbanSyn</b>	39810	0	0	7539	0.090	0.654	4.084	0.167	0.915	0.970	0.985
<b>320×1024</b>	<b>MixSyn</b>	39810	21260	153000	7539	<b>0.087</b>	<b>0.644</b>	<b>4.079</b>	<b>0.166</b>	<b>0.920</b>	0.970	0.985

TABLE IX  
ABLATION STUDY ON MODELS WITH PARAMS AND COMPUTATIONAL COMPLEXITIES(GFLOPS).

Method	Model	Size	Params(M)	Flops(G)	Error Metric				Accuracy Metric		
					abs_rel	sq_rel	rmse	rmse_log	a1	a2	a3
<b>MonoViT [2]</b>	small	320×1024	33.63	159.14	0.093	0.671	4.202	0.169	0.912	0.969	<b>0.985</b>
<b>Lite-mono [1]</b>	8M	320×1024	8.76	29.88	0.097	0.710	4.309	0.174	0.905	0.967	0.984
<b>Back2Color</b>	VAN0	320×1024	5.17	17.64	0.094	0.706	4.257	0.171	0.910	0.969	0.984
<b>Back2Color</b>	VAN1	320×1024	18.61	51.48	0.090	0.664	4.139	0.168	0.915	0.970	0.984
<b>Back2Color</b>	VAN2	320×1024	31.32	76.01	<b>0.087</b>	<b>0.644</b>	4.079	0.166	<b>0.920</b>	0.970	<b>0.985</b>
<b>Back2Color</b>	VAN3	320×1024	49.5	114.63	<b>0.087</b>	0.653	<b>4.068</b>	<b>0.165</b>	0.919	<b>0.971</b>	<b>0.985</b>
<b>Back2Color</b>	VAN0	384×1280	5.17	17.64	0.093	0.676	4.169	0.171	0.911	0.969	0.984
<b>Back2Color</b>	VAN1	384×1280	18.61	51.48	0.090	0.664	4.102	0.168	0.917	<b>0.970</b>	0.984
<b>Back2Color</b>	VAN2	384×1280	31.32	76.01	<b>0.086</b>	<b>0.629</b>	<b>4.054</b>	<b>0.165</b>	<b>0.920</b>	<b>0.970</b>	<b>0.985</b>
<b>Back2Color</b>	VAN3	384×1280	49.5	114.63	0.087	0.652	4.062	<b>0.165</b>	<b>0.920</b>	<b>0.970</b>	0.984



Fig. 13. The visual results of joint training with different synthetic datasets. The model trained with SHIFT jointly learns more features of pedestrians while treating glass as transparent entities.

Firstly, it’s undeniable that our method, through joint training with synthetic datasets, achieves clearer boundaries and more detailed depth estimations compared to training solely with unsupervised depth estimation, as depicted in Fig. 11. The model successfully captures features of obstacles that unsupervised learning alone struggles to discern. For instance, roadside barriers(Fig.11, Col 2), which run parallel to the direction of vehicle movement and remain unchanged across multiple frames, pose challenges for unsupervised methods but are accurately predicted with the aid of synthetic depths.

Synthetic depths are dense and accurate, providing crucial information about these obstacles.

Furthermore, the characteristics of synthetic datasets are also learned by the network. For example, as shown in Fig.9, the SHIFT dataset has two characteristics compared to the vKITTI2. Firstly, it contains a amount of pedestrians, which are often difficult to estimate correctly in unsupervised depth estimation, typically resulting in partial depth disappearance or blurring, as seen in the estimation results of DIFFNet in the Fig.12, Row 1. When using our method with the SHIFT dataset, the network learns the knowledge of estimating pedestrian, achieving clear and accurate estimation of pedestrian depth, which is impressive.

This point can also be inferred from predicted depth of transparent objects, such as glass. As shown in Fig.9, in the vKITTI2, transparent objects like glass are treated as solid entities and can be detected, resulting in smooth surfaces in Depth. However, in the SHIFT, transparent objects are considered penetrable targets, leading to discontinuous depth in these regions. This difference in Synthetic dataset definitions is perfectly reflected in the training, as shown in Fig.13, Row 2. Models trained with the SHIFT dataset recognize and penetrate through vehicle windows, whereas those trained with the vKITTI2 dataset perceive them as flat surfaces.

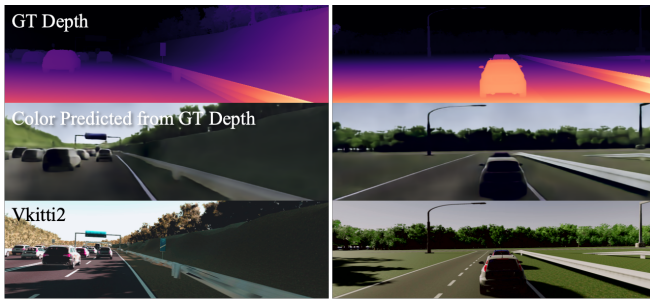


Fig. 14. An experiment predicting color from ground truth (GT) depth showed that shadows and road markings vanished, undetectable in the depth image. See Discussion for details.

## F. Discussion

### Why can the network transform information beyond depth?

In Fig. 3, Syn-to-Real images exhibit excessive detail surpassing information in depth, such as tree shadows and lane markings. We attribute this to the Color-Depth-Color process, where depth, predicted from color, retains texture details (such as subtle gradient changes at some boundaries). Consequently, the Color Net can recover such gradient changes from the depth map. To validate, we directly trained the network to predict color images from synthesized depth in the synthetic dataset (Fig. 14). The absence of lane markings and shadows in the restored color images confirms our hypothesis.

In practice, the ambiguity is significantly reduced by the strong appearance consistency within a target domain (e.g., KITTI or Cityscapes), enabling the depth-to-color network to learn a stable, domain-specific mapping.

## V. CONCLUSION

This paper presented Back2Color, an unsupervised monocular depth estimation framework for robust depth perception in urban driving scenarios. By learning a depth-to-color mapping from real-world data and transferring it to synthetic scenes, the proposed method effectively reduces the synthetic-to-real appearance gap and improves depth estimation under real traffic conditions. In addition, an uncertainty-aware temporal-spatial fusion strategy is introduced to handle non-rigid motion and occlusions, leading to more reliable depth predictions in dynamic environments. Experimental results on standard driving benchmarks demonstrate consistent performance improvements with favorable computational efficiency, highlighting the practicality of the proposed approach for vision-based perception in intelligent transportation systems.

## REFERENCES

- [1] N. Zhang, F. Nex, G. Vosselman, and N. Kerle, "Lite-mono: A lightweight cnn and transformer architecture for self-supervised monocular depth estimation," in *Proceedings of the IEEE/CVF Conference on Computer Vision and Pattern Recognition*, 2023, pp. 18 537–18 546.
- [2] C. Zhao, Y. Zhang, M. Poggi, F. Tosi, X. Guo, Z. Zhu, G. Huang, Y. Tang, and S. Mattoccia, "Monovit: Self-supervised monocular depth estimation with a vision transformer," in *2022 International Conference on 3D Vision (3DV)*. IEEE, 2022, pp. 668–678.
- [3] C. B. Hochberg and J. E. Hochberg, "Familiar size and the perception of depth," *The Journal of Psychology*, vol. 34, no. 1, pp. 107–114, 1952.
- [4] S. Gokturk, H. Yalcin, and C. Bamji, "A time-of-flight depth sensor - system description, issues and solutions," in *2004 Conference on Computer Vision and Pattern Recognition Workshop*, 2004, pp. 35–35.
- [5] N. Li, C. P. Ho, J. Xue, L. W. Lim, G. Chen, Y. H. Fu, and L. Y. T. Lee, "A progress review on solid-state lidar and nanophotonics-based lidar sensors," *Laser & Photonics Reviews*, vol. 16, no. 11, p. 2100511, 2022.
- [6] Y. Kim, H. Jung, D. Min, and K. Sohn, "Deep monocular depth estimation via integration of global and local predictions," *IEEE transactions on Image Processing*, vol. 27, no. 8, pp. 4131–4144, 2018.
- [7] H. Sheng, S. Zhang, X. Cao, Y. Fang, and Z. Xiong, "Geometric occlusion analysis in depth estimation using integral guided filter for light-field image," *IEEE Transactions on Image Processing*, vol. 26, no. 12, pp. 5758–5771, 2017.
- [8] J. Lin, X. Ji, W. Xu, and Q. Dai, "Absolute depth estimation from a single defocused image," *IEEE Transactions on Image Processing*, vol. 22, no. 11, pp. 4545–4550, 2013.
- [9] Z. Li, W. Ye, D. Wang, F. X. Creighton, R. H. Taylor, G. Venkatesh, and M. Unberath, "Temporally consistent online depth estimation in dynamic scenes," in *Proceedings of the IEEE/CVF winter conference on applications of computer vision*, 2023, pp. 3018–3027.
- [10] Q.-T. Luong and O. D. Faugeras, "The fundamental matrix: Theory, algorithms, and stability analysis," *International journal of computer vision*, vol. 17, no. 1, pp. 43–75, 1996.
- [11] R. Blake and H. Wilson, "Binocular vision," *Vision research*, vol. 51, no. 7, pp. 754–770, 2011.
- [12] S. Ingle and M. Phute, "Tesla autopilot: semi autonomous driving, an uptick for future autonomy," *International Research Journal of Engineering and Technology*, vol. 3, no. 9, pp. 369–372, 2016.
- [13] C. Godard, O. Mac Aodha, M. Firman, and G. J. Brostow, "Digging into self-supervised monocular depth estimation," in *Proceedings of the IEEE/CVF international conference on computer vision*, 2019, pp. 3828–3838.
- [14] Y. Hu, J. Gao, J. Dong, B. Fan, and H. Liu, "Exploring rich semantics for open-set action recognition," *IEEE Transactions on Multimedia*, vol. 26, pp. 5410–5421, 2024.
- [15] M. Cordts, M. Omran, S. Ramos, T. Rehfeld, M. Enzweiler, R. Benenson, U. Franke, S. Roth, and B. Schiele, "The cityscapes dataset for semantic urban scene understanding," in *Proceedings of the IEEE conference on computer vision and pattern recognition*, 2016, pp. 3213–3223.
- [16] Y. Cabon, N. Murray, and M. Humenberger, "Virtual kitti 2," 2020.
- [17] G. Ros, L. Sellart, J. Materzynska, D. Vazquez, and A. M. Lopez, "The synthia dataset: A large collection of synthetic images for semantic segmentation of urban scenes," in *Proceedings of the IEEE conference on computer vision and pattern recognition*, 2016, pp. 3234–3243.
- [18] X. Huang, X. Cheng, Q. Geng, B. Cao, D. Zhou, P. Wang, Y. Lin, and R. Yang, "The apolloscape dataset for autonomous driving," in *Proceedings of the IEEE conference on computer vision and pattern recognition workshops*, 2018, pp. 954–960.
- [19] A. Dosovitskiy, G. Ros, F. Codevilla, A. Lopez, and V. Koltun, "Carla: An open urban driving simulator," in *Conference on robot learning*. PMLR, 2017, pp. 1–16.
- [20] J. K. Haas, "A history of the unity game engine," *Diss. Worcester Polytechnic Institute*, vol. 483, no. 2014, p. 484, 2014.
- [21] A. Sanders, *An introduction to Unreal engine 4*. CRC Press, 2016.
- [22] A. Gurrarn, A. F. Tuna, F. Shen, O. Urfalioglu, and A. M. López, "Monocular depth estimation through virtual-world supervision and real-world sfm self-supervision," *IEEE Transactions on Intelligent Transportation Systems*, vol. 23, no. 8, pp. 12 738–12 751, 2021.
- [23] A. Geiger, P. Lenz, and R. Urtasun, "Are we ready for autonomous driving? the kitti vision benchmark suite," in *2012 IEEE conference on computer vision and pattern recognition*. IEEE, 2012, pp. 3354–3361.
- [24] S. Yun, D. Han, S. J. Oh, S. Chun, J. Choe, and Y. Yoo, "Cutmix: Regularization strategy to train strong classifiers with localizable features," in *Proceedings of the IEEE/CVF international conference on computer vision*, 2019, pp. 6023–6032.
- [25] Y. Zhu, R. Ren, W. Dong, X. Li, and G. Shi, "Tsudepth: Exploring temporal symmetry-based uncertainty for unsupervised monocular depth estimation," *Neurocomputing*, p. 128165, 2024.
- [26] T. Sun, M. Segu, J. Postels, Y. Wang, L. Van Gool, B. Schiele, F. Tombari, and F. Yu, "SHIFT: a synthetic driving dataset for continuous multi-task domain adaptation," in *Proceedings of the IEEE/CVF Conference on Computer Vision and Pattern Recognition (CVPR)*, June 2022, pp. 21 371–21 382.
- [27] J. L. Gómez, M. Silva, A. Seoane, A. Borrás, M. Noriega, G. Ros, J. A. Iglesias-Guitian, and A. M. López, "All for one, and one for all: Urbansyn dataset, the third musketeer of synthetic driving scenes," 2023.

- [28] D. Eigen, C. Puhrsch, and R. Fergus, "Depth map prediction from a single image using a multi-scale deep network," *Advances in neural information processing systems*, vol. 27, 2014.
- [29] C. Godard, O. Mac Aodha, and G. J. Brostow, "Unsupervised monocular depth estimation with left-right consistency," in *Proceedings of the IEEE conference on computer vision and pattern recognition*, 2017, pp. 270–279.
- [30] T. Zhou, M. Brown, N. Snavely, and D. G. Lowe, "Unsupervised learning of depth and ego-motion from video," in *Proceedings of the IEEE conference on computer vision and pattern recognition*, 2017, pp. 1851–1858.
- [31] V. Guizilini, R. Ambrus, S. Pillai, A. Raventos, and A. Gaidon, "3d packing for self-supervised monocular depth estimation," in *Proceedings of the IEEE/CVF conference on computer vision and pattern recognition*, 2020, pp. 2485–2494.
- [32] J. Yan, H. Zhao, P. Bu, and Y. Jin, "Channel-wise attention-based network for self-supervised monocular depth estimation," in *2021 International Conference on 3D Vision (3DV)*. IEEE, 2021, pp. 464–473.
- [33] X. Lyu, L. Liu, M. Wang, X. Kong, L. Liu, Y. Liu, X. Chen, and Y. Yuan, "Hr-depth: High resolution self-supervised monocular depth estimation," in *Proceedings of the AAAI Conference on Artificial Intelligence*, vol. 35, no. 3, 2021, pp. 2294–2301.
- [34] H. Zhou, D. Greenwood, and S. Taylor, "Self-supervised monocular depth estimation with internal feature fusion," *arXiv preprint arXiv:2110.09482*, 2021.
- [35] M. He, L. Hui, Y. Bian, J. Ren, J. Xie, and J. Yang, "Ra-depth: Resolution adaptive self-supervised monocular depth estimation," in *European Conference on Computer Vision*. Springer, 2022, pp. 565–581.
- [36] Z. Li, X. Wang, X. Liu, and J. Jiang, "Binsformer: Revisiting adaptive bins for monocular depth estimation," *IEEE Transactions on Image Processing*, vol. 33, pp. 3964–3976, 2024.
- [37] A. Vaswani, N. Shazeer, N. Parmar, J. Uszkoreit, L. Jones, A. N. Gomez, Ł. Kaiser, and I. Polosukhin, "Attention is all you need," *Advances in neural information processing systems*, vol. 30, 2017.
- [38] A. Dosovitskiy, L. Beyer, A. Kolesnikov, D. Weissenborn, X. Zhai, T. Unterthiner, M. Dehghani, M. Minderer, G. Heigold, S. Gelly *et al.*, "An image is worth 16x16 words: Transformers for image recognition at scale," *arXiv preprint arXiv:2010.11929*, 2020.
- [39] Z. Liu, Y. Lin, Y. Cao, H. Hu, Y. Wei, Z. Zhang, S. Lin, and B. Guo, "Swin transformer: Hierarchical vision transformer using shifted windows," in *Proceedings of the IEEE/CVF international conference on computer vision*, 2021, pp. 10012–10022.
- [40] R. Ranftl, A. Bochkovskiy, and V. Koltun, "Vision transformers for dense prediction," in *Proceedings of the IEEE/CVF international conference on computer vision*, 2021, pp. 12 179–12 188.
- [41] A. Varma, H. Chawla, B. Zonooz, and E. Arani, "Transformers in self-supervised monocular depth estimation with unknown camera intrinsics," *arXiv preprint arXiv:2202.03131*, 2022.
- [42] Y. Lee, J. Kim, J. Willette, and S. J. Hwang, "Mpvit: Multi-path vision transformer for dense prediction," in *Proceedings of the IEEE/CVF Conference on Computer Vision and Pattern Recognition*, 2022, pp. 7287–7296.
- [43] C. Zhang, G. Meng, B. Fan, K. Tian, Z. Zhang, S. Xiang, and C. Pan, "Reusable architecture growth for continual stereo matching," *IEEE Transactions on Pattern Analysis and Machine Intelligence*, 2024.
- [44] K. Swami, A. Muduli, U. Gurrain, and P. Bajpai, "Do what you can, with what you have: Scale-aware and high quality monocular depth estimation without real world labels," in *Proceedings of the IEEE/CVF Conference on Computer Vision and Pattern Recognition*, 2022, pp. 988–997.
- [45] Y. Ganin and V. Lempitsky, "Unsupervised domain adaptation by back-propagation," in *International conference on machine learning*. PMLR, 2015, pp. 1180–1189.
- [46] Y. Zhao, S. Kong, D. Shin, and C. Fowlkes, "Domain decluttering: Simplifying images to mitigate synthetic-real domain shift and improve depth estimation," in *Proceedings of the IEEE/CVF Conference on Computer Vision and Pattern Recognition*, 2020, pp. 3330–3340.
- [47] P. Isola, J.-Y. Zhu, T. Zhou, and A. A. Efros, "Image-to-image translation with conditional adversarial networks," in *Proceedings of the IEEE conference on computer vision and pattern recognition*, 2017, pp. 1125–1134.
- [48] A. Atapour-Abarghouei and T. P. Breckon, "Real-time monocular depth estimation using synthetic data with domain adaptation via image style transfer," in *Proceedings of the IEEE conference on computer vision and pattern recognition*, 2018, pp. 2800–2810.
- [49] S.-W. Huang, C.-T. Lin, S.-P. Chen, Y.-Y. Wu, P.-H. Hsu, and S.-H. Lai, "Auggan: Cross domain adaptation with gan-based data augmentation," in *Proceedings of the European Conference on Computer Vision (ECCV)*, 2018, pp. 718–731.
- [50] J. L. Gómez, G. Villalonga, and A. M. López, "Co-training for unsupervised domain adaptation of semantic segmentation models," *Sensors*, vol. 23, no. 2, p. 621, 2023.
- [51] C. Zheng, T.-J. Cham, and J. Cai, "T2net: Synthetic-to-realistic translation for solving single-image depth estimation tasks," in *Proceedings of the European conference on computer vision (ECCV)*, 2018, pp. 767–783.
- [52] L. Zhang, A. Rao, and M. Agrawala, "Adding conditional control to text-to-image diffusion models," in *Proceedings of the IEEE/CVF International Conference on Computer Vision*, 2023, pp. 3836–3847.
- [53] R. Upadhyay, H. Zhang, Y. Ba, E. Yang, B. Gella, S. Jiang, A. Wong, and A. Kadambi, "Enhancing diffusion models with 3d perspective geometry constraints," *ACM Transactions on Graphics (TOG)*, vol. 42, no. 6, pp. 1–15, 2023.
- [54] H. Liu, F. Jin, H. Zeng, H. Pu, and B. Fan, "Image enhancement guided object detection in visually degraded scenes," *IEEE Transactions on Neural Networks and Learning Systems*, pp. 1–14, 2023.
- [55] T.-W. Hui, "Rm-depth: Unsupervised learning of recurrent monocular depth in dynamic scenes," in *Proceedings of the IEEE/CVF Conference on Computer Vision and Pattern Recognition*, 2022, pp. 1675–1684.
- [56] Y. Zhu, W. Dong, L. Li, J. Wu, X. Li, and G. Shi, "Robust depth completion with uncertainty-driven loss functions," in *Proceedings of the AAAI Conference on Artificial Intelligence*, vol. 36, no. 3, 2022, pp. 3626–3634.
- [57] Q. Ning, W. Dong, X. Li, J. Wu, and G. Shi, "Uncertainty-driven loss for single image super-resolution," *Advances in Neural Information Processing Systems*, vol. 34, pp. 16 398–16 409, 2021.
- [58] R. Ranftl, K. Lasinger, D. Hafner, K. Schindler, and V. Koltun, "Towards robust monocular depth estimation: Mixing datasets for zero-shot cross-dataset transfer," *IEEE transactions on pattern analysis and machine intelligence*, vol. 44, no. 3, pp. 1623–1637, 2020.
- [59] L. Yang, B. Kang, Z. Huang, X. Xu, J. Feng, and H. Zhao, "Depth anything: Unleashing the power of large-scale unlabeled data," *arXiv preprint arXiv:2401.10891*, 2024.
- [60] J. Bae, S. Moon, and S. Im, "Deep digging into the generalization of self-supervised monocular depth estimation," in *Proceedings of the AAAI conference on artificial intelligence*, vol. 37, no. 1, 2023, pp. 187–196.
- [61] A. Paszke, S. Gross, F. Massa, A. Lerer, J. Bradbury, G. Chanan, T. Killeen, Z. Lin, N. Gimelshein, L. Antiga *et al.*, "Pytorch: An imperative style, high-performance deep learning library," *Advances in neural information processing systems*, vol. 32, 2019.
- [62] D. P. Kingma and J. Ba, "Adam: A method for stochastic optimization," *arXiv preprint arXiv:1412.6980*, 2014.
- [63] M.-H. Guo, C.-Z. Lu, Z.-N. Liu, M.-M. Cheng, and S.-M. Hu, "Visual attention network," *Computational Visual Media*, vol. 9, no. 4, pp. 733–752, 2023.
- [64] M. Klingner, J.-A. Termöhlen, J. Mikolajczyk, and T. Fingscheidt, "Self-supervised monocular depth estimation: Solving the dynamic object problem by semantic guidance," in *Computer Vision—ECCV 2020: 16th European Conference, Glasgow, UK, August 23–28, 2020, Proceedings, Part XX 16*. Springer, 2020, pp. 582–600.
- [65] R. Wang, Z. Yu, and S. Gao, "Planedepth: Self-supervised depth estimation via orthogonal planes," in *Proceedings of the IEEE/CVF Conference on Computer Vision and Pattern Recognition*, 2023, pp. 21 425–21 434.
- [66] V. Casser, S. Pirk, R. Mahjourian, and A. Angelova, "Depth prediction without the sensors: Leveraging structure for unsupervised learning from monocular videos," in *Proceedings of the AAAI conference on artificial intelligence*, vol. 33, no. 01, 2019, pp. 8001–8008.
- [67] Y. Chen, C. Schmid, and C. Sminchisescu, "Self-supervised learning with geometric constraints in monocular video: Connecting flow, depth, and camera," in *Proceedings of the IEEE/CVF International Conference on Computer Vision*, 2019, pp. 7063–7072.
- [68] A. Gordon, H. Li, R. Jonschkowski, and A. Angelova, "Depth from videos in the wild: Unsupervised monocular depth learning from unknown cameras," in *Proceedings of the IEEE/CVF International Conference on Computer Vision*, 2019, pp. 8977–8986.
- [69] H. Li, A. Gordon, H. Zhao, V. Casser, and A. Angelova, "Unsupervised monocular depth learning in dynamic scenes," in *Conference on Robot Learning*. PMLR, 2021, pp. 1908–1917.
- [70] S. Lee, S. Im, S. Lin, and I. S. Kweon, "Learning monocular depth in dynamic scenes via instance-aware projection consistency," in *Proceedings of the AAAI Conference on Artificial Intelligence*, vol. 35, no. 3, 2021, pp. 1863–1872.